

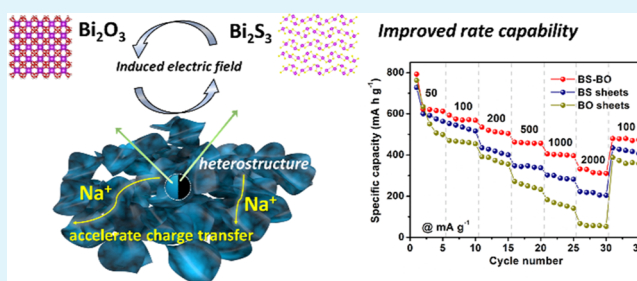
Heterostructured Bi_2S_3 – Bi_2O_3 Nanosheets with a Built-In Electric Field for Improved Sodium Storage

Wen Luo,^{†,‡} Feng Li,[†] Qidong Li,[†] Xuanpeng Wang,[†] Wei Yang,[†] Liang Zhou,^{†,§} and Liqiang Mai^{*,†,§}[†]State Key Laboratory of Advanced Technology for Materials Synthesis and Processing, Wuhan University of Technology, Wuhan 430070, China[‡]Laboratory of Chemistry and Physics: Multiscale Approach to Complex Environments (LCP-A2MC), Institute of Jean Barriol, University of Lorraine, Metz 57070, France[§]Department of Chemistry, University of California, Berkeley, California 94720, United States

Supporting Information

ABSTRACT: Constructing novel heterostructures has great potential in tuning the physical/chemical properties of functional materials for electronics, catalysis, as well as energy conversion and storage. In this work, heterostructured Bi_2S_3 – Bi_2O_3 nanosheets (BS–BO) have been prepared through an easy water-bath approach. The formation of such unique BS–BO heterostructures was achieved through a controllable thioacetamide-directed surfactant-assisted reaction process. Bi_2O_3 sheets and Bi_2S_3 sheets can be also prepared through simply modifying the synthetic recipe. When employed as the sodium-ion battery anode material, the resultant BS–BO displays a reversible capacity of $\sim 630 \text{ mA h g}^{-1}$ at 100 mA g^{-1} . In addition, the BS–BO demonstrates improved rate capability and enhanced cycle stability compared to its Bi_2O_3 sheets and Bi_2S_3 sheets counterparts. The improved electrochemical performance can be ascribed to the built-in electric field in the BS–BO heterostructure, which effectively facilitates the charge transport. This work would shed light on the construction of novel heterostructures for high-performance sodium-ion batteries and other energy-related devices.

KEYWORDS: Bi_2S_3 – Bi_2O_3 nanosheets, heterostructure, built-in electric field, sodium-ion batteries, anode



INTRODUCTION

The demand for low-cost, high-efficiency energy storage technologies is greatly increasing to utilize renewable energy resources and reduce environmental pollution. Rechargeable lithium-ion batteries (LIBs) are undoubtedly one of the most successful candidates among various energy storage devices.^{1–3} Recently, sodium-ion batteries (SIBs) are emerging as a promising alternative to commercial LIBs because of the abundant, inexpensive sodium resources and their similar redox chemistry to LIBs.⁴ Nevertheless, because the ionic radius of Na^+ ions is much larger (102 pm) than that of Li^+ ions (76 pm), most investigated electrode materials suffer from huge volume expansion during sodiation/de-sodiation processes, resulting in low specific capacity and limited cycle life.^{5–8} Hence, the pursuit of SIB electrode materials with high specific capacity and stable cycling performance remains a major challenge.

Metal chalcogenides, such as Fe_3S_4 ,⁹ FeSe_2 ,¹⁰ Sb_2S_3 ,¹¹ and Sb_2Se_3 ,¹² have attracted considerable attention in sodium storage because of their high specific capacity and intriguing layered structure. Bi_2S_3 is a well-known layered p-type semiconductor with a band gap of approximately 1.3 eV, and it displays enormous potential in thermoelectrics,^{13,14} photo-

catalysis,^{15–18} photodetectors,^{19–21} as well as electrochemical energy conversion and storage.^{22–24} For sodium storage, Bi_2S_3 is capable to display gravimetric and volumetric capacities of 625 mA h g^{-1} and $4250 \text{ mA h cm}^{-3}$, respectively.^{25,26} Bi_2O_3 is also a typical layered semiconductor with a band gap of 2.8 eV (n-type semiconductor).²⁷ For sodium storage, the Bi_2O_3 possesses a high theoretical capacity of 690 mA h g^{-1} .^{28,29} Despite their high theoretical capacities, the sodium storage performances of Bi_2O_3 and Bi_2S_3 are usually unsatisfactory. For instance, the $\text{Bi}_2\text{O}_3/\text{C}$ composite displayed a short life span of only 20 cycles.²⁹ The $\text{Bi}_2\text{O}_3/\text{rGO}$ nanocomposite exhibited a capacity retention of 70.2% after 200 cycles.³⁰ The binder-free and flexible $\text{Bi}_2\text{O}_3/\text{C}$ delivered a specific capacity of 430 mA h g^{-1} after 200 cycles.³¹ The $\text{Bi}_2\text{S}_3/\text{CNT}$ nanocomposite delivered a capacity of only 84.8 mA h g^{-1} after 60 cycles at 60 mA g^{-1} .³² Further enhancement of the sodium storage performance of Bi-based anodes still remains a great challenge.

Constructing heterostructures composed of at least two components with different band gaps has great potential in

Received: January 28, 2018

Accepted: February 6, 2018

Published: February 6, 2018

tuning the physical/chemical properties of functional materials.^{33–36} Because of the unique interface effect, many advantages have been realized in heterostructures in various energy storage devices. Of particular note is the fact that Guo et al. proposed a conceptual model of SnS/SnO₂ heterostructures with built-in electric fields and thus boosted charge transfer capability.³⁷ Using an ultrathin Bi₂MoO₆ nanosheet as an example, the same group interpreted the electric-field effect based on density functional theory (DFT) calculations.³⁸ Recently, Yu et al. confirmed that unbalanced charge distribution would occur within crystals and induce built-in electric fields, leading to boosted lithium-ion transfer dynamics.³⁹ Herein, inspired by the built-in electric field effect and enhanced charge transfer in heterostructured materials, we designed Bi₂S₃–Bi₂O₃ (BS–BO) heterostructures and explored them in SIB application. Detailed characterizations demonstrated that the formation of such unique BS–BO heterostructures was achieved through a controllable thioacetamide (TAA)-directed surfactant-assisted reaction process. Bi₂O₃ sheets and Bi₂S₃ sheets can also be prepared by simply modifying the synthetic recipe. The BS–BO, as an anode for SIBs, delivers a reversible capacity of 630 mA h g⁻¹ at 100 mA g⁻¹. Besides, the BS–BO also demonstrates better cycling stability and rate capability compared with the Bi₂O₃ sheet and Bi₂S₃ sheet counterparts. The improved sodium storage performance makes the BS–BO heterostructures a promising anode for SIBs, and the facile synthetic approach also provides new insights into the construction of novel heterostructures.

EXPERIMENTAL SECTION

Synthetic Procedures. For the synthesis of BS–BO heterostructures, 0.243 g of Bi(NO₃)₃·5H₂O and 0.125 mL of HNO₃ (14 M) were first added into 5 mL of deionized water, leading to the formation of a milky suspension. Then, a sulfurization agent was prepared by dissolving 0.125 g of hexadecyl trimethyl ammonium bromide (CTAB) and 0.075 g of TAA in 60 mL of deionized water through ultrasonication. The abovementioned milky suspension was added into the sulfurization solution dropwise with constant stirring. The mixture was incubated at 30 °C for 3 h. The final product was collected by centrifugation and thoroughly washed with deionized water and ethanol three times. The synthesis of Bi₂S₃ sheets is similar to that of BS–BO heterostructures except that a higher amount of TAA (0.375 g) was used. If no TAA was used in the synthesis, Bi₂O₃ sheets were obtained through the incubation of milky suspension at 30 °C for 3 h.

Characterization. Field-emission scanning electron microscopy (FESEM) images were collected with a JEOL-7100F microscope. X-ray diffraction (XRD) patterns were obtained with a D8 ADVANCE X-ray diffractometer using Cu K α radiation ($\lambda = 1.5418$ Å). Transmission electron microscopy (TEM) and high-resolution TEM (HRTEM) images were recorded by using a JEM-2100F STEM/EDS microscope. The Fourier transform infrared (FTIR) instrument used was a Nicolet 60-SXB spectrometer. X-ray photoelectron spectroscopy (XPS) measurements were conducted using a VG MultiLab 2000 instrument. CHNS element analysis was conducted on a Vario EL cube Elementar.

Electrochemical Measurements. The sodium storage behaviors were characterized by an assembly of CR2016 coin cells. The working electrodes were prepared by mixing the as-prepared products, carboxyl methyl cellulose, and acetylene black at a weight ratio of 80:10:10. The slurry was casted onto an aluminum (Al) foil and completely dried in a vacuum oven at 70 °C overnight. The average mass loading was about 1.3 mg cm⁻². A sodium metal foil was utilized as the counter electrode and the reference electrode; a glass fiber membrane was used as the separator. The electrolyte was a solution of 1 M trifluoromethanesulfonate (NaCF₃SO₃) in diethyleneglycol dimethylether. Galvanostatic

discharge–charge tests were conducted on a multichannel battery testing system (LAND CT2001A) at a potential range of 0.01–3.0 V versus Na⁺/Na. Cyclic voltammetry (CV) was tested with an Autolab CHI760E electrochemical workstation. Electrochemical impedance spectroscopy (EIS) measurements were performed on an Autolab PGSTAT 302N electrochemical workstation over the frequency range of 100 kHz–0.01 Hz. All abovementioned measurements were performed on at room temperature.

RESULTS AND DISCUSSION

Microstructure and Morphology Characterization.

The schematic illustration for the construction of various nanostructures is briefly depicted in Figure 1. First, Bi₂O₃

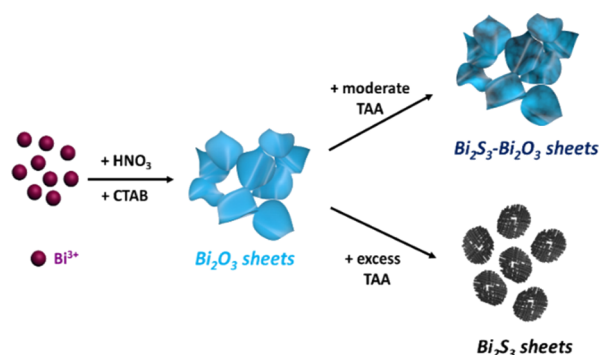


Figure 1. Schematic illustration of the synthesis process of Bi₂O₃ sheets, BS–BO heterostructured sheets, and Bi₂S₃ sheets.

sheets are synthesized through a facile water-bath process at room temperature. For the synthesis of BS–BO heterostructures, TAA is utilized as the sulfurization agent and the Bi₂O₃ sheet is used as the precursor. The BS–BO heterostructured sheets can be achieved by using an appropriate amount of sulfurization agent and suitable sulfurization time. When an excess amount of sulfurization agents is employed, the Bi₂O₃ sheets transform into Bi₂S₃ sheets completely.

Figures 2a and S1 depict the XRD patterns of Bi₂O₃, BS–BO heterostructure, and Bi₂S₃. As shown in Figure 2a, all the diffraction peaks of the Bi₂O₃ precursor can be indexed to the cubic phase Bi₂O₃ (JCPDS 052-1007). The peaks exhibit broad full width at half maximum and weak intensity, implying the low-crystalline feature of Bi₂O₃. This result agrees well with previous literature that highly crystallized cubic phase Bi₂O₃ is difficult to be achieved at room temperature without further annealing.²⁸ After moderate sulfurization, the diffraction peaks for Bi₂O₃ still remain; meanwhile, new peaks belonging to the orthorhombic phase Bi₂S₃ (JCPDS 17-0320) appear. The XRD pattern of Bi₂S₃ is presented in Figure S1, confirming the successful synthesis of pure orthorhombic phase bismuth sulfide (JCPDS 17-0320). No obvious peaks from Bi₂O₃ can be observed, suggesting that the Bi₂O₃ is completely converted into Bi₂S₃ with an enough amount of the sulfurization agent.

The FTIR spectra of the Bi₂O₃ precursor and the BS–BO heterostructure are presented in Figure 2b. The bands detected at 533, 711, and 957 cm⁻¹ can be observed in both Bi₂O₃ and BS–BO. For BS–BO, the emerging new band at 619 cm⁻¹ can be assigned to Bi–S caused by the partial transformation to Bi₂S₃.^{35,40} It is worth mentioning that the bands located at 1384 and 1626 cm⁻¹ are attributed to C–OH and C–N stretching vibrations, respectively. These bands indicate the existence of CTAB species and H₂O absorbed on the surface of the final products.⁴¹

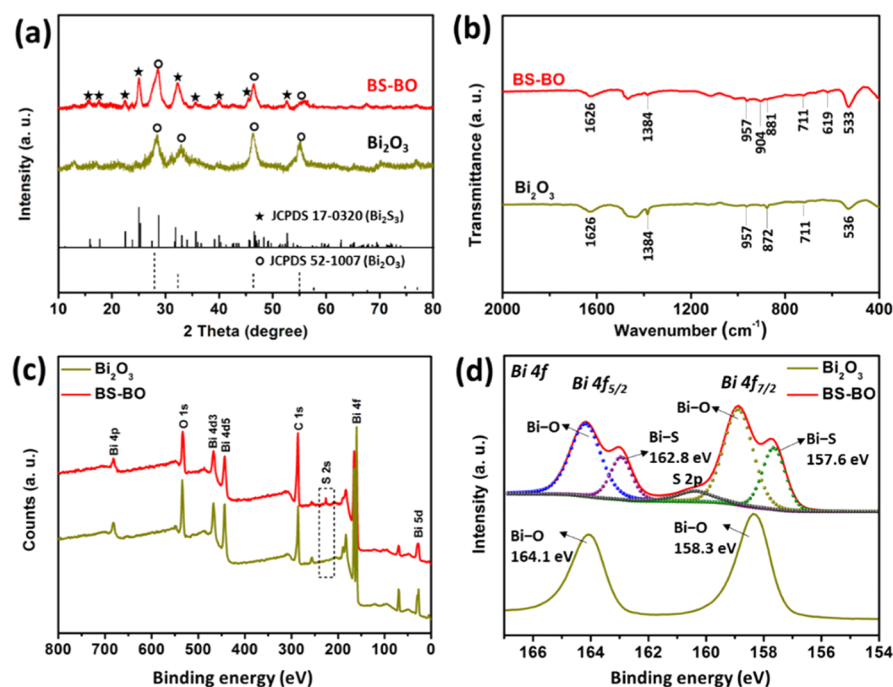


Figure 2. (a) XRD patterns of Bi_2O_3 sheets and BS–BO heterostructures. (b) FTIR spectra of Bi_2O_3 sheets and BS–BO heterostructures. (c) XPS survey spectra of Bi_2O_3 sheets and BS–BO heterostructures. (d) High-resolution Bi 4f XPS spectra of Bi_2O_3 sheets and BS–BO heterostructures.

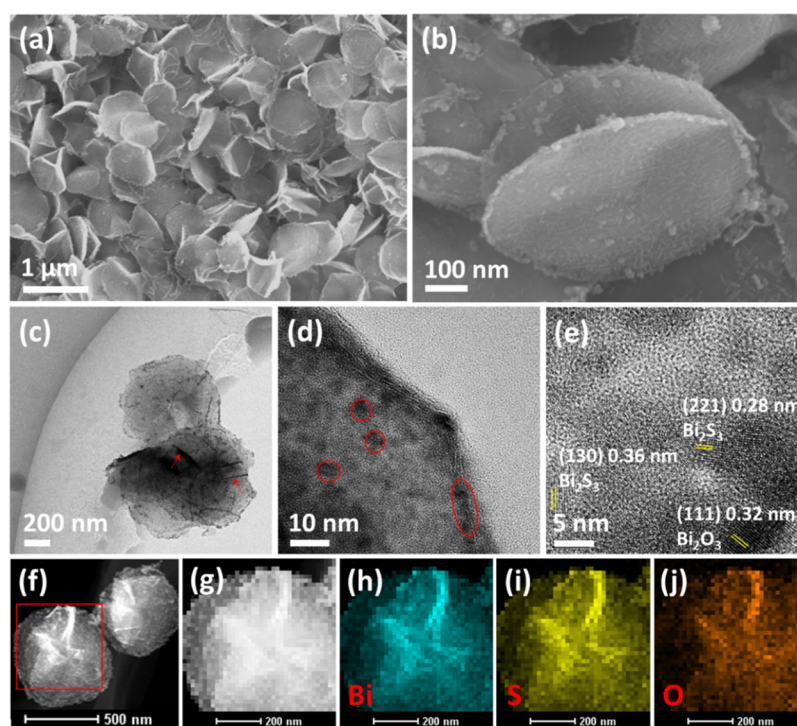


Figure 3. Morphology characterizations of BS–BO heterostructures. SEM images (a,b), TEM images (c,d), HRTEM image (e), STEM images (f,g), and corresponding elemental mapping images (from the red rectangle area in (f) of Bi (h), S (i), O (j) of BS–BO heterostructured sheets.

XPS survey spectra of Bi_2O_3 and BS–BO heterostructure are provided in Figure 2c. Signals from Bi, O, and C elements can be observed in the XPS spectrum of Bi_2O_3 . After sulfuration, the S 2s peak at 225.1 eV can be detected in BS–BO, confirming the successful incorporation of S. Figure 2d shows the high-resolution XPS spectra of Bi_2O_3 and BS–BO heterostructure. For Bi_2O_3 , the two strong peaks located at 164.1 and 158.3 eV can be ascribed to Bi $4f_{7/2}$ and Bi $4f_{5/2}$,

respectively. For BS–BO, the peaks with a binding energy of 162.8 and 157.6 eV are correlated with Bi $4f_{7/2}$ and Bi $4f_{5/2}$ in Bi_2S_3 , respectively. Moreover, the Bi $4f_{7/2}$ and Bi $4f_{5/2}$ peaks for Bi_2O_3 shift toward higher energies by approximately 0.5 eV, which is because of the coupling effect resulted from the strong chemical bonding between Bi_2O_3 and Bi_2S_3 .⁴² The peak centered at 160.4 eV in BS–BO is ascribed to S 2p transition,⁴³ which further confirms the formation of BS–BO hetero-

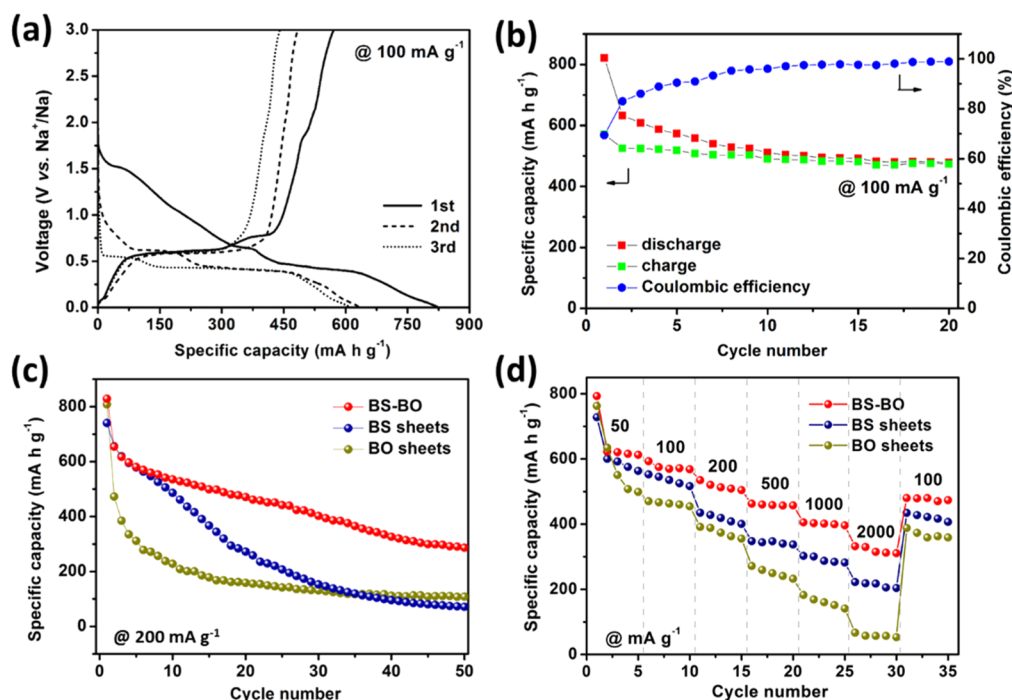


Figure 4. Electrochemical performances of BS-BO, Bi_2S_3 , and Bi_2O_3 electrodes for sodium storage. (a) Typical charge–discharge profiles of BS-BO at a current density of 100 mA g^{-1} for the initial three cycles. (b) Cycling performance of BS-BO at 100 mA g^{-1} for 20 cycles. (c) Cycling performance of BS-BO, Bi_2S_3 , and Bi_2O_3 sheets at a current density of 200 mA g^{-1} . (d) Rate performances of BS-BO, Bi_2S_3 , and Bi_2O_3 sheets at different current densities.

structures. In addition, the high-resolution C 1s (Figure S2a) and O 1s (Figure S2b) XPS spectra of BS-BO indicate the presence of adsorbed species, such as CTAB and H_2O , which are consistent with the FTIR results. CHNS elemental analysis results are shown in Table S1; the weight percentage of sulfur in BS-BO is determined to be 14.83%. The abovementioned results reveal that the orthorhombic Bi_2S_3 and cubic Bi_2O_3 coexist in the BS-BO heterostructured composite.

The morphologies and microstructures of the BS-BO, Bi_2O_3 , and Bi_2S_3 were characterized by FESEM and TEM. The Bi_2O_3 displays a uniform sheet-like structure with ultrathin thickness and quite smooth surface (Figure S3). The Bi_2O_3 sheets are wrinkled rather than flat, which avoids their stacking (Figure S3a). The thickness of the Bi_2O_3 sheets is less than 20 nm (Figure S3b). TAA was utilized as the sulfurization agent to convert Bi_2O_3 into Bi_2S_3 .⁴⁴ The amount of the sulfurization agent plays a vital role in the synthesis. If an excess amount of TAA was used, micrometer-sized Bi_2S_3 sheets can be obtained (Figure S4a). The Bi_2S_3 sheets show a coarse surface (Figure S4b). With the use of an appropriate amount of TAA, a BS-BO heterostructured composite can be achieved (Figure 3). The as-synthesized BS-BO well inherits the sheet-like morphology of the Bi_2O_3 precursor; however, it shows a coarser surface with less wrinkles (Figure 3a). The diameter and thickness of the BS-BO nanosheets are determined to be around 600 nm and tens of nanometer, respectively (Figure 3b). When further examined under TEM, the wrinkles can be clearly observed on the surface of BS-BO (indicated by arrows in Figure 3c). The heterostructure feature can be clearly recognized by the contrast in the TEM image (Figure 3d), in which the Bi_2S_3 shows darker mass-thickness contrast (highlighted with the red circle) while the Bi_2O_3 shows brighter contrast. A typical HRTEM image of BS-BO is provided in Figure 3e. The atomic spacing of 0.28 and 0.36 nm correspond

to the (221) and (130) planes of orthorhombic Bi_2S_3 , respectively. The lattice fringe of 0.32 nm is correlated with the (111) planes of cubic Bi_2O_3 . The elemental mapping images under TEM (Figure 3g–j) confirm the uniform distribution of Bi, S, and O elements within BS-BO nanosheets. The abovementioned results indicate that sheet-like BS-BO heterostructures have been successfully constructed.

Sodium Storage Performance. The sodium storage behaviors of BS-BO, Bi_2S_3 , and Bi_2O_3 sheets were examined in CR2016 coin cells. CV was first employed to investigate electrochemical performance of BS-BO (Figure S5). During the first cathodic scan, a broad reduction peak located at 0.51 V can be observed. This peak splits into two peaks at around 0.31 and 0.68 V in the subsequent scans, suggesting the evolution might be associated with irreversible activation. The first oxidation process of BS-BO is featured by two peaks at around 0.64 and 0.78 V, which are different from the typical oxidation peaks of Bi_2O_3 (Figure S6) and Bi_2S_3 anodes (Figure S7). Because of the homogeneous distribution at nanoscale and strong chemical interactions between Bi_2S_3 and Bi_2O_3 , the electrochemical redox process of BS-BO cannot be directly recognized as the simple overlap of its two counterparts. As CV cycles proceed, the profiles of BS-BO change slightly with less pronounced current responses.

The first three galvanostatic discharge–charge profiles of BS-BO, Bi_2O_3 , and Bi_2S_3 at a current density of 100 mA g^{-1} are shown in Figures 4a, S8, and S9, respectively. The first discharge and charge capacities for BS-BO are 821 and 571 mA h g^{-1} , corresponding to a relatively low initial Coulombic efficiency of 69.5%. The irreversible capacity loss might be caused by the generation of solid electrolyte interphase films. In detail, the initial discharge plateau of BS-BO at around 1.55 V representing the activation process is almost lost in the

subsequent cycles. Two apparent discharge plateaus are located at 0.65 and 0.45 V, agreeing well with the CV profiles. These plateaus are associated with the formation of metallic Bi and Na₃Bi alloys, respectively. The discharge plateaus are consistent with the ex situ studies on bismuth-based anode materials.²⁹ The main charge plateau is located at 0.61 V, which is ascribed to the dealloying process from Na₃Bi to metallic Bi and the oxidation of Bi to Bi³⁺.²⁵ The cycling performance and the corresponding Coulombic efficiency of BS–BO at a current density of 100 mA g⁻¹ are shown in Figure 4b. A large capacity loss occurs in the first cycle. The second discharge capacity can reach 630 mA h g⁻¹, which is slightly higher than the theoretic capacity of Bi₂S₃ (625 mA h g⁻¹) and approaches the theoretical capacity of Bi₂O₃ (690 mA h g⁻¹). After 20 cycles, the BS–BO is capable of delivering a discharge capacity of 477 mA h g⁻¹, corresponding to a capacity retention of 76% (against the second discharge capacity). Additionally, the Coulombic efficiency increases significantly during the initial six cycles and stabilizes at around 98% in the subsequent processes.

For comparison, the cycling performances of BS–BO, Bi₂S₃, and Bi₂O₃ at a current density of 200 mA g⁻¹ are provided in Figure 4c. The capacity of Bi₂O₃ decays fast from the start of cycling. After 50 cycles, the capacity of Bi₂O₃ is merely around 109 mA h g⁻¹. A similar severe capacity decay is also observed in Bi₂S₃. With respect to BS–BO, the capacity decay is mild. The capacity retentions for BS–BO, Bi₂S₃, and Bi₂O₃ sheets (against second discharge capacity) are 43, 11, and 2%, respectively. The great enhancement in capacity retention confirms the advantages of the novel BS–BO heterostructure.

To further demonstrate the good sodium storage performance of BS–BO, the rate performances of the three samples were measured with the applied current densities increasing from 50 to 2000 mA g⁻¹ and then reducing back to 100 mA g⁻¹ (Figure 4d). As can be seen clearly, the BS–BO exhibits a remarkably improved rate performance at a variety of current densities. The reversible discharge capacities are approximately 620, 574, 518, 460, 404, and 314 mA h g⁻¹ at 50, 100, 200, 500, 1000, and 2000 mA g⁻¹, respectively. Besides, when the current density reduces to 100 mA g⁻¹, an average capacity of 468 mA h g⁻¹ can be restored for the BS–BO. In contrast, both Bi₂S₃ and Bi₂O₃ sheets suffer from severe capacity loss at a high rate and exhibit poor capacity recovery ability. These results demonstrate that the constructed BS–BO heterostructure is beneficial to the rate capability when compared with the Bi₂S₃ or Bi₂O₃ counterparts.

EIS measurements were performed to investigate the kinetic characteristic and charge transfer resistance of various electrodes. All typical Nyquist plots provided in Figure S10 exhibit a slope line in the low frequency region and a semicircle in the high–medium frequency region. It can be clearly observed that the semicircle diameter for BS–BO is much smaller than those for Bi₂S₃ and Bi₂O₃ sheets. After simulation, the charge transfer resistance (R_{ct}) values for the BS–BO, Bi₂S₃, and Bi₂O₃ sheets are calculated to be 17.8, 42.6, and 209.2 Ω , respectively. The EIS results confirm the enhanced charge transport in BS–BO heterostructures.

The improved sodium storage performance originates from the novel design of BS–BO heterostructures with three distinctive merits. First, a built-in electric field within the heterostructure can accelerate the charge transfer. A possible mechanism of the evolution of built-in electric fields in BS–BO is illustrated in Figure 5. The Bi₂O₃ is a n-type semiconductor

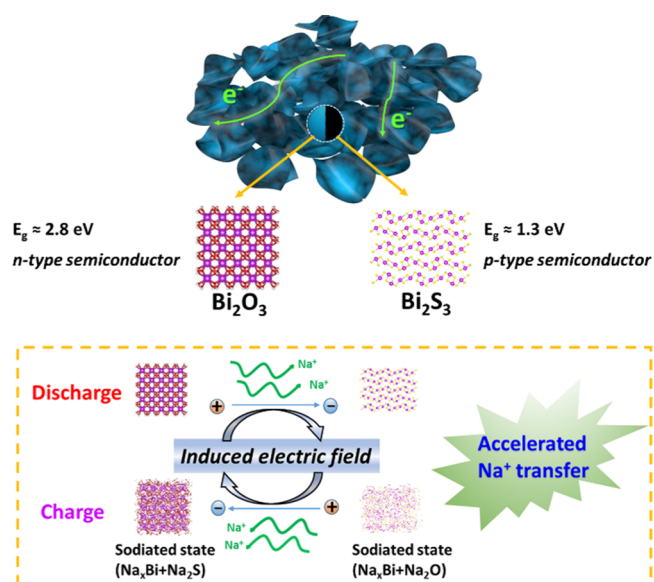


Figure 5. Schematic illustration of the accelerated charge transfer resulted from an induced electric field mechanism in BS–BO heterostructures.

featured with a relative wide band gap of 2.8 eV,^{13,14} while Bi₂S₃ is a typical p-type semiconductor with a narrow band gap (1.3 eV).²⁸ In the BS–BO heterostructure, BS–BO p–n heterojunctions formed at the interface can induce a built-in electric field with a direction from Bi₂O₃ ($E_g \approx 2.8$ eV) to Bi₂S₃ ($E_g \approx 1.3$ eV).⁴⁵ It can be anticipated that during the discharge process, this electric field can facilitate the immigration of Na⁺ ions. On the other hand, Bi₂O₃ is converted into Na_xBi and Na₂O after full sodiation. Meanwhile, Bi₂S₃ is sodiated into Na_xBi and Na₂S.³⁷ As evidenced in the literature, more Na⁺ ions might be released at the sulfide area (Bi₂S₃-domained area) after full de-sodiation on account of its higher reversibility relative to some oxides (Bi₂O₃-domained area).^{37,46} Consequently, when subject to the charge process, an electric field could be formed with a direction from Bi₂S₃ to Bi₂O₃ owing to the potential difference, which will promote the transfer of Na⁺ ions. Therefore, within the BS–BO heterostructure, the induced built-in electric field would provide a driving force for Na⁺ ions and remarkably improve the charge transfer kinetics, resulting in good rate capability. Secondly, the strong chemical interaction between Bi₂O₃ and Bi₂S₃ would be helpful to the elastic effects of the nanostructures upon sodiation/de-sodiation.⁴⁷ Last but not the least, the thin nanosheets design can effectively decrease the diffusion pathway of Na⁺ ions, which further promotes the electrochemical kinetics. In a word, the synergetic effect of enhanced charge transfer kinetic, strong chemical interaction, and nanoscale size design makes BS–BO nanosheets a promising material for the high-performance sodium-ion battery anode.

CONCLUSIONS

In summary, BS–BO heterostructured nanosheets have been constructed via an easy water-bath approach. The present method has been demonstrated to be a TAA-directed surfactant-assisted process. When applied in sodium storage, the BS–BO heterostructure displays a promising performance: it delivers a reversible discharge capacity of 630 mA h g⁻¹ at 100 mA g⁻¹ with relative good stability. Moreover, the BS–BO heterostructure exhibits improved rate capability compared to

Bi_2S_3 and Bi_2O_3 counterparts, which can be originated from the synergetic effect of enhanced charge transfer in the heterostructures, strong chemical interaction, and nanoscale size design. This work suggests that the construction of novel heterostructures can be a promising approach toward high-performance sodium-ion battery and related energy storage applications.

■ ASSOCIATED CONTENT

📄 Supporting Information

The Supporting Information is available free of charge on the ACS Publications website at DOI: 10.1021/acami.8b01613.

XRD pattern of Bi_2S_3 sheets; XPS studies of C and O elements in BS–BO; SEM images of Bi_2O_3 sheets and Bi_2S_3 sheets; CHNS test results of BS–BO; CV profiles of various electrodes for the initial three cycles; typical charge–discharge curves of Bi_2S_3 sheets and Bi_2O_3 sheets for the initial three cycles; and Nyquist plots of various electrodes (PDF)

(PDF)

■ AUTHOR INFORMATION

Corresponding Author

*E-mail: mlq518@whut.edu.cn.

ORCID

Liang Zhou: 0000-0001-6756-3578

Liqiang Mai: 0000-0003-4259-7725

Author Contributions

W.L. and F.L. contributed equally to this work. The manuscript was written through contributions of all authors. All authors have given approval to the final version of the manuscript.

Notes

The authors declare no competing financial interest.

■ ACKNOWLEDGMENTS

This work was supported by the National Key Research and Development Program of China (2016YFA0202603), the National Basic Research Program of China (2013CB934103), the Programme of Introducing Talents of Discipline to Universities (B17034), the National Natural Science Foundation of China (51521001, 21673171, 51502226), the National Natural Science Fund for Distinguished Young Scholars (51425204), and the Fundamental Research Funds for the Central Universities (WUT: 2016-JL-004, 2016III001, 2016III002, 2017III009, 2017III008), L.M. gratefully acknowledged financial support from China Scholarship Council (no. 201606955096).

■ REFERENCES

- (1) Armand, M.; Tarascon, J.-M. Building better batteries. *Nature* **2008**, *451*, 652–657.
- (2) Goodenough, J. B.; Park, K.-S. The Li-ion rechargeable battery: a perspective. *J. Am. Chem. Soc.* **2013**, *135*, 1167–1176.
- (3) Mai, L.; Tian, X.; Xu, X.; Chang, L.; Xu, L. Nanowire electrodes for electrochemical energy storage devices. *Chem. Rev.* **2014**, *114*, 11828–11862.
- (4) Kim, S.-W.; Seo, D.-H.; Ma, X.; Ceder, G.; Kang, K. Electrode materials for rechargeable sodium-ion batteries: potential alternatives to current lithium-ion batteries. *Adv. Energy Mater.* **2012**, *2*, 710–721.
- (5) Pan, H.; Hu, Y.-S.; Chen, L. Room-temperature stationary sodium-ion batteries for large-scale electric energy storage. *Energy Environ. Sci.* **2013**, *6*, 2338–2360.

- (6) Cao, Y.; Xiao, L.; Sushko, M. L.; Wang, W.; Schwenzler, B.; Xiao, J.; Nie, Z.; Saraf, L. V.; Yang, Z.; Liu, J. Sodium ion insertion in hollow carbon nanowires for battery applications. *Nano Lett.* **2012**, *12*, 3783–3787.

- (7) Kundu, D.; Talaie, E.; Duffort, V.; Nazar, L. F. The emerging chemistry of sodium ion batteries for electrochemical energy storage. *Angew. Chem., Int. Ed.* **2015**, *54*, 3431–3448.

- (8) Luo, W.; Zhang, P.; Wang, X.; Li, Q.; Dong, Y.; Hua, J.; Zhou, L.; Mai, L. Antimony nanoparticles anchored in three-dimensional carbon network as promising sodium-ion battery anode. *J. Power Sources* **2016**, *304*, 340–345.

- (9) Li, Q.; Wei, Q.; Zuo, W.; Huang, L.; Luo, W.; An, Q. Y.; Pelenovich, V. O.; Mai, L.; Zhang, Q. Greigite Fe_3S_4 as a new anode material for high-performance sodium-ion batteries. *Chem. Sci.* **2017**, *8*, 160–164.

- (10) Zhang, K.; Hu, Z.; Liu, X.; Tao, Z.; Chen, J. FeSe_2 microspheres as a high-performance anode material for Na-ion batteries. *Adv. Mater.* **2015**, *27*, 3305–3309.

- (11) Yu, D. Y.W.; Prikhodchenko, P. V.; Mason, C. W.; Batabyal, S. K.; Gun, J.; Sladkevich, S.; Medvedev, A. G.; Lev, O. High-capacity antimony sulphide nanoparticle-decorated graphene composite as anode for sodium-ion batteries. *Nat. Commun.* **2013**, *4*, 2922.

- (12) Luo, W.; Calas, A.; Tang, C.; Li, F.; Zhou, L.; Mai, L. Ultralong Sb_2Se_3 nanowire based free-standing membrane anode for lithium/sodium ion batteries. *ACS Appl. Mater. Interfaces* **2016**, *8*, 35219–35226.

- (13) Biswas, K.; Zhao, L.-D.; Kanatzidis, M. G. Tellurium-free thermoelectric: the anisotropic *n*-type semiconductor Bi_2S_3 . *Adv. Energy Mater.* **2012**, *2*, 634–638.

- (14) Ge, Z.-H.; Zhang, B.-P.; Shang, P.-P.; Li, J.-F. Control of anisotropic electrical transport property of Bi_2S_3 thermoelectric polycrystals. *J. Mater. Chem.* **2011**, *21*, 9194–9200.

- (15) Pineda, E.; Nicho, M. E.; Nair, P. K.; Hu, H. Optoelectronic properties of chemically deposited Bi_2S_3 thin films and the photovoltaic performance of $\text{Bi}_2\text{S}_3/\text{P}_3\text{OT}$ solar cells. *Sol. Energy* **2012**, *86*, 1017–1022.

- (16) Yu, H.; Huang, J.; Zhang, H.; Zhao, Q.; Zhong, X. Nanostructure and charge transfer in $\text{Bi}_2\text{S}_3\text{-TiO}_2$ heterostructures. *Nanotechnology* **2014**, *25*, 215702.

- (17) Brahim, R.; Bessekhoud, Y.; Bouguelia, A.; Trari, M. Visible light induced hydrogen evolution over the heterosystem $\text{Bi}_2\text{S}_3/\text{TiO}_2$. *Catal. Today* **2007**, *122*, 62–65.

- (18) Kim, J.; Kang, M. High photocatalytic hydrogen production over the band gap-tuned urchin-like Bi_2S_3 -loaded TiO_2 composites system. *Int. J. Hydrogen Energy* **2012**, *37*, 8249–8256.

- (19) Chen, G.; Yu, Y.; Zheng, K.; Ding, T.; Wang, W.; Jiang, Y.; Yang, Q. Fabrication of ultrathin Bi_2S_3 nanosheets for high-performance, flexible, visible-NIR photodetectors. *Small* **2015**, *11*, 2848–2855.

- (20) Konstantatos, G.; Levina, L.; Tang, J.; Sargent, E. H. Sensitive solution-processed Bi_2S_3 nanocrystalline photodetectors. *Nano Lett.* **2008**, *8*, 4002–4006.

- (21) Tahir, A. A.; Ehsan, M. A.; Mazhar, M.; Wijayantha, K. G. U.; Zeller, M.; Hunter, A. D. Photoelectrochemical and photoresponsive properties of Bi_2S_3 nanotube and nanoparticle thin films. *Chem. Mater.* **2010**, *22*, 5084–5092.

- (22) Ni, J.; Zhao, Y.; Liu, T.; Zheng, H.; Gao, L.; Yan, C.; Li, L. Strongly coupled Bi_2S_3 @CNT hybrids for robust lithium storage. *Adv. Energy Mater.* **2014**, *4*, 1400798.

- (23) Zhao, Y.; Gao, D.; Ni, J.; Gao, L.; Yang, J.; Li, Y. One-pot facile fabrication of carbon-coated Bi_2S_3 nanomeshes with efficient Li-storage capability. *Nano Res.* **2014**, *7*, 765–773.

- (24) Li, W.-J.; Han, C.; Chou, S.-L.; Wang, J.-Z.; Li, Z.; Kang, Y.-M.; Liu, H.-K.; Dou, S.-X. Graphite-nanoplate-coated Bi_2S_3 composite with high-volume energy density and excellent cycle life for room-temperature sodium-sulfide batteries. *Chem.—Eur. J.* **2016**, *22*, 590–597.

- (25) Yang, W.; Wang, H.; Liu, T.; Gao, L. A Bi_2S_3 @CNT nanocomposite as anode material for sodium ion batteries. *Mater. Lett.* **2016**, *167*, 102–105.
- (26) Sun, W.; Rui, X.; Zhang, D.; Jiang, Y.; Sun, Z.; Liu, H.; Dou, S. Bismuth sulfide: A high-capacity anode for sodium-ion batteries. *J. Power Sources* **2016**, *309*, 135–140.
- (27) Zhou, L.; Wang, W.; Xu, H.; Sun, S.; Shang, M. Bi_2O_3 hierarchical nanostructures: controllable synthesis, growth mechanism, and their application in photocatalysis. *Chem.—Eur. J.* **2009**, *15*, 1776–1782.
- (28) Deng, Z.; Liu, T.; Chen, T.; Jiang, J.; Yang, W.; Guo, J.; Zhao, J.; Wang, H.; Gao, L. Enhanced electrochemical performances of Bi_2O_3 /rGO nanocomposite via chemical bonding as anode materials for lithium ion batteries. *ACS Appl. Mater. Interfaces* **2017**, *9*, 12469–12477.
- (29) Kim, M.-K.; Yu, S.-H.; Jin, A.; Kim, J.; Ko, I.-H.; Lee, K.-S.; Mun, J.; Sung, Y.-E. Bismuth oxide as a high capacity anode material for sodium-ion batteries. *Chem. Commun.* **2016**, *52*, 11775–11778.
- (30) Nithya, C. Bi_2O_3 @ reduced graphene oxide nanocomposite: An anode material for sodium-ion storage. *ChemPlusChem* **2015**, *80*, 1000–1006.
- (31) Yin, H.; Cao, M.-L.; Yu, X.-X.; Zhao, H.; Shen, Y.; Li, C.; Zhu, M.-Q. Self-standing Bi_2O_3 nanoparticles/carbon nanofiber hybrid films as a binder-free anode for flexible sodium-ion batteries. *Mater. Chem. Front.* **2017**, *1*, 1615–1621.
- (32) Yang, W.; Wang, H.; Liu, T.; Gao, L. A Bi_2S_3 @ CNT nanocomposite as anode material for sodium ion batteries. *Mater. Lett.* **2016**, *167*, 102–105.
- (33) Gong, Y.; Lin, J.; Wang, X.; Shi, G.; Lei, S.; Lin, Z.; Zou, X.; Ye, G.; Vajtai, R.; Yakobson, B. I.; Terrones, H.; Terrones, M.; Tay, B. K.; Lou, J.; Pantelides, S. T.; Liu, Z.; Zhou, W.; Ajayan, P. M. Vertical and in-plane heterostructures from WS_2 / MoS_2 monolayers. *Nat. Mater.* **2014**, *13*, 1135–1142.
- (34) Gao, X.; Wu, H. B.; Zheng, L.; Zhong, Y.; Hu, Y.; Lou, X. W. D. Formation of mesoporous heterostructured BiVO_4 / Bi_2S_3 hollow discoids with enhanced photoactivity. *Angew. Chem., Int. Ed.* **2014**, *53*, 5917–5921.
- (35) Liu, T.; Zhao, Y.; Gao, L.; Ni, J. Engineering Bi_2O_3 - Bi_2S_3 heterostructure for superior lithium storage. *Sci. Rep.* **2015**, *5*, 9307.
- (36) Cai, F.-G.; Yang, F.; Jia, Y.-F.; Ke, C.; Cheng, C.-H.; Zhao, Y. Bi_2S_3 -modified TiO_2 nanotube arrays: easy fabrication of heterostructure and effective enhancement of photoelectrochemical property. *J. Mater. Sci.* **2013**, *48*, 6001–6007.
- (37) Zheng, Y.; Zhou, T.; Zhang, C.; Mao, J.; Liu, H.; Guo, Z. Boosted charge transfer in SnS/SnO_2 heterostructures: toward high rate capability for sodium-ion batteries. *Angew. Chem., Int. Ed.* **2016**, *55*, 3408–3413.
- (38) Zheng, Y.; Zhou, T.; Zhao, X.; Pang, W. K.; Gao, H.; Li, S.; Zhou, Z.; Liu, H.; Guo, Z. Atomic interface engineering and electric-field effect in ultrathin Bi_2MoO_6 nanosheets for superior lithium ion storage. *Adv. Mater.* **2017**, *29*, 1700396.
- (39) Yan, C.; Zhu, Y.; Li, Y.; Fang, Z.; Peng, L.; Zhou, X.; Chen, G.; Yu, G. Local built-in electric field enabled in carbon-doped Co_3O_4 nanocrystals for superior lithium-ion storage. *Adv. Funct. Mater.* **2018**, *28*, 1705951.
- (40) Zhang, L.; Li, N.; Jiu, H.; Zhang, Q. Solvothermal synthesis of reduced graphene oxide- Bi_2S_3 nanorod composites with enhanced photocatalytic activity under visible light irradiation. *J. Mater. Sci.: Mater. Electron.* **2016**, *27*, 2748–2753.
- (41) Zhao, Y.; Liu, T.; Xia, H.; Zhang, L.; Jiang, J.; Shen, M.; Ni, J.; Gao, L. Branch-structured Bi_2S_3 -CNT hybrids with improved lithium storage capability. *J. Mater. Chem. A* **2014**, *2*, 13854–13858.
- (42) Gao, M.-R.; Yu, S.-H.; Yuan, J.; Zhang, W.; Antonietti, M. Poly (ionic liquid)-mediated morphogenesis of bismuth sulfide with a tunable band gap and enhanced electrocatalytic properties. *Angew. Chem., Int. Ed.* **2016**, *128*, 13004–13008.
- (43) Tian, L.; Tan, H. Y.; Vittal, J. J. Morphology-controlled synthesis of Bi_2S_3 nanomaterials via single-and multiple-source approaches. *Cryst. Growth Des.* **2007**, *8*, 734–738.
- (44) Li, L.; Sun, N.; Huang, Y.; Qin, Y.; Zhao, N.; Gao, J.; Li, M.; Zhou, H.; Qi, L. Topotactic transformation of single-crystalline precursor discs into disc-like Bi_2S_3 nanorod networks. *Adv. Funct. Mater.* **2008**, *18*, 1194–1201.
- (45) Ma, D.-K.; Guan, M.-L.; Liu, S.-S.; Zhang, Y.-Q.; Zhang, C.-W.; He, Y.-X.; Huang, S.-M. Controlled synthesis of olive-shaped Bi_2S_3 / BiVO_4 microspheres through a limited chemical conversion route and enhanced visible-light-responding photocatalytic activity. *Dalton Trans.* **2012**, *41*, 5581–5586.
- (46) Cai, K.; Song, M.-K.; Cairns, E. J.; Zhang, Y. Nanostructured Li_2S -C composites as cathode material for high-energy lithium/sulfur batteries. *Nano Lett.* **2012**, *12*, 6474–6479.
- (47) Ni, J.; Fu, S.; Wu, C.; Maier, J.; Yu, Y.; Li, L. Self-supported nanotube arrays of sulfur-doped TiO_2 enabling ultrastable and robust sodium storage. *Adv. Mater.* **2016**, *28*, 2259–2265.